Supporting Information for
"Catalysis and Chemical Mechanisms of Calcite Dissolution in Seawater"
Adam V. Subhas, Jess F. Adkins, Nick E. Rollins, John Naviaux, Jonathan Erez, and William M. Berelson

Calculating a Reactive Layer Thickness using Secondary Ion Mass Spectrometry (SIMS)

Data Collection

6-8 large (300x300 μm) ^{13}C-labeled calcite grains were embedded in 1-inch epoxy discs. Discs were then polished to 0.25 μm and reacted for 48 hours in an experimental setup similar to the dissolution experiments described in the Methods section and in Subhas et al. (2015). The alkalinity contribution of the epoxy resin to alkalinity over the course of the 48-hour experiment was minimal (at most a 4 μeq/kg increase). Omegas for the supersaturated and undersaturated experiments were 1.32±0.03 and 0.96±0.02. After reaction, discs were rinsed thoroughly with methanol and air-dried for 30 minutes before covering and storing in the dark. Methanol was used to avoid further reaction with the surface of the calcites, and for its low vapor pressure (thus low potential for carbon contamination during SIMS analyses).

Secondary Ion Mass Spectrometer profiles were collected on a Cameca 7f SIMS instrument. Carbon isotope ratios were collected in positive ion mode using a Cesium beam. Mg/Ca ratios were collected as ^{24}Mg/^{40}Ca in negative ion mode using an oxygen beam. A correction factor of 1.23 was applied to collected Mg/Ca ratios to account for the relative natural abundances of these isotopes. Isotope fractionation factors for both carbon and Mg/Ca incorporation into calcite were ignored as they are on the order of a permil relative and thus insignificant at our level of precision. Pertinent tuning parameters can be found in Table S1. Before measuring isotopic profiles, the epoxy discs were sputter-coated with 20 nm gold to ensure surface conductivity. Coated discs were then loaded into the sample evacuation chamber for ∼30 hours to degas the epoxy. Dynamic transfer optics setting (DTOS) was turned off to minimize edge effects on the profile ion beam.

Profiles were collected on at least 3 different grains, with at least 2 different spots on each grain for a total of at least 6 total analyses per experiment. Profiles on unreacted grains were collected in the same way without reaction in seawater. SIMS profiles in the main text show carbon isotope profiles for each epoxy disc. Solid lines are the mean of all profiles, and shaded regions depict the standard deviation of all profiles collected under each experimental condition. Proflies for Mg/Ca are shown in Figure S1; profiles of carbon isotope ratios are shown in Fig.1 in the main text. Carbon isotope profiles are generally cleaner and show greater separation between supersaturated and undersaturated experiments. Mg/Ca profiles are noisier, and there is less distinction between the supersaturated and undersaturated experiments. This difference can be explained by two mechanisms. First, fewer counts of Mg than Carbon-13 led to a greater relative error in each cycle, calculated using Poisson statistics. Especially deeper in the profile, this counting error manifests as noisy profiles. Second, cesium and oxygen ion beams have different properties and thus mixing dynamics during the sputtering process. The oxygen beam

was more energetic and produced rougher pits compared to the cesium beam (Figure S2).

Plots of SIMS profiles were corrected for the thickness of gold, which was burned through in about 12 cycles for C isotopes and 7 cycles for Mg/Ca. The appearance of $CaCO_3$ underlying the gold coating was diagnosed by an increase in the raw counts of C and Ca ions. In order to convert mass spectrometer cycles into vertical depth, the pit depths of all profiles were measured using a profilometer, and applied as a mean value to all profiles. This mean profile depth was used to convert the number of SIMS analysis cycles to depth, corrected for the thickness of the gold coating. Examples of pit geometries are shown in Figure S2. Pits were in general shallower and rougher in topography for the oxygen beam (Mg/Ca) than the cesium beam (C isotope) profiles. This difference in profile shape helps to explain the different profile shapes seen between Figure 1 in the main text and Figure S1. Poorer resolution in the depth direction, and a more energetic oxygen beam, lead to poorer distinction between magnesium signatures in the supersaturated and undersaturated experiments in Figure S1.

Analysis and Data Reduction

Because SIMS sputtering is an energetic process, profiles shown in Figure 1 and S1 represent mixing curves, where excavated calcite is continually mixed down into the solid during the sputtering process. The number of moles in the reactive calcite layer was estimated using both cation and anion mass balances by integrating the amount of ^{12}C and Mg throughout the profile. Both carbon isotope and Mg/Ca intensity ratios were converted to intensity fractions for each ratio cycle, and multiplied by the number of moles in each cycle to give a number of either Mg or ^{12}C moles in each cycle. These values were then summed to give a total number of Mg^{2+} and ^{12}C moles added in the solid:

$$
\begin{aligned}
{}^{12}\mathrm{C}_{tot} &= \sum_{0}^{i} z_i \cdot \left(\frac{SA_{raster} \cdot \rho_{calcite}}{mm_{calcite}} \right) \cdot f_i^{12}; \\
{\mathrm{Mg}^{2+}}_{tot} &= \sum_{0}^{i} z_i \cdot \left(\frac{SA_{raster} \cdot \rho_{calcite}}{mm_{calcite}} \right) \cdot f_i^{\mathrm{Mg}^{2+}};
\end{aligned}
\tag{1}
$$

where the sum was taken over all cycles i in the profiles. z_i is the mean thickness of calcite sputtered in each cycle, estimated by dividing the measured pit depth by the total number of cycles. f_i^{12} is the intensity fraction of $^{12}C/(^{13}C + {}^{12}C)$ measured in SIMS cycle i; $f_i^{\mathrm{Mg}^{2+}}$ is the intensity fraction of Mg^{2+} measured in each SIMS cycle. SA_{raster} is the SIMS raster area (50x50 μm^2); $\rho_{calcite} = 2.6 \cdot 10^6$ g m^{-3} is the density of calcite and $mm_{calcite} = 100$ g mol^{-1} is the molar mass of calcite. For carbon isotope balance, any ^{12}C enrichment above the control run was assumed to represent new calcite added. Thus, the mean integrated number of moles from the control experiment was subtracted from the experimental profiles. For Mg/Ca balance, an Mg/Ca ratio of 0.08 was assumed for the newly precipitated solid (Mucci and Morse, 1984; Sun et al., 2015). Thus to calculate the number of moles of new calcite added we divided by this ratio:

$$\begin{aligned} \mathrm{CaCO_{3(^{12}C,new)}} &= {}^{12}\mathrm{C}_{tot}; \\ \mathrm{CaCO_{3(Mg,new)}} &= {\mathrm{Mg^{2+}}}_{tot} \cdot \left.\frac{\mathrm{Ca}}{\mathrm{Mg}}\right|_{solid,eq}. \end{aligned} \tag{2}$$

Here, $\mathrm{Ca/Mg}_{solid,eq} = 1/0.08$ is taken from measurements of about 8 mole % magnesium incorporated into calcite grown in equilibrium with modern seawater (Mucci and Morse, 1984). Estimates for the total moles of new/exchanged calcite, as calculated by carbon and magnesium mass balances, as well as effective reactive layer thicknesses, are presented in LayerThickness. Effective layer thicknesses (z_{eff}) were estimated by converting the total moles of new calcite to a volume of calcite ($\rho_{calcite} = 2.63 gcm^{-3}$) and dividing by the sims raster surface area (50x50 $\mu\mathrm{m}^2$):

$$\begin{aligned} z_{eff,^{12}\mathrm{C}} &= \mathrm{CaCO_{3(^{12}C,new)}} \cdot \frac{mm_{calcite}}{\rho_{calcite} \cdot SA_{raster}}; \\ z_{eff,Mg} &= \mathrm{CaCO_{3(Mg,new)}} \cdot \frac{mm_{calcite}}{\rho_{calcite} \cdot SA_{raster}}. \end{aligned} \tag{3}$$

The values for $z_{eff,Mg}$ are lower than $z_{eff,^{12}\mathrm{C}}$. We do not know the precipitated phase in our system, and thus there is significant uncertainty in the newly precipitated solid Mg/Ca ratio. For example, there is experimental evidence that in seawater of Mg/Ca = 5, aragonite is favored to precipitate even on calcite seeds (Sun et al., 2015; Morse et al., 1997). The distribution coefficient of $\mathrm{Mg^{2+}}$ into aragonite is significantly lower than that in calcite by at least one order of magnitude (Zhong and Mucci, 1989). An Mg/Ca of 0.08 is thus an upper bound on the amount of Mg incorporated into our calcite. Using it in Eq.(2) represents a lower limit on the total carbonate precipitation in these experiments, and helps explain why layer thicknesses using Mg/Ca mass balance are thinner than those from carbon isotope mass balance.

Finally, we ground-truthed the SIMS data using the precipitation ($\Omega = 1.3$) experiment and compared to literature values of precipitation rate. At $\Omega = 1.3$, Zhong and Mucci (1989) measured a calcite precipitation rate of 1 μmol $\mathrm{m^{-2}\ hr^{-1}}$. Mulitplying this rate by the molar mass and dividing by the density of calcite gives a rate of 0.037 nanometers of calcite precipitated per hour. Over a 48 hour period, we should thus expect about 1.8 nm of calcite precipitated onto our SIMS disks. However, we measured that about 3-9 nm of ^{12}C-calcite was added in our $\Omega = 1.3$ experiments (Table S2). The discrepancy between the net amount of calcite added to the surface and the amount of ^{12}C measured on the SIMS can be attributed to calcite exchange due to dissolution-precipitation reactions at the calcite surface.

Assuming a linear relationship between precipitation rate and Ω, similar to Eq. 1 in the main text, there should be a 30% imbalance in gross precipitation and dissolution rates at $\Omega = 1.3$. Dissolution and reprecipitation will exchange solid ^{13}C with seawater ^{12}C, above and beyond the net accumulation of calcite. To estimate the amount of ^{12}C added in such dissolution-precipitation reactions, we used the box model described below, but modified it to add calcite to the reactive surface at a rate of 1 μmol $\mathrm{m^{-2}\ hr^{-1}}$. We also set the balance of dissolution to precipitation of $R_{precip}/R_{diss} = 1.3$. The results of this model, and a comparison to the model run in its "dissolution" configuration, are shown in Figure S3. As seen in Figure S3b, about 2.1 nanometers of calcite was added under precipitation conditions. Figure S3a further shows that about 4.4 nanometers of ^{12}C-calcite was added to the solid through a combination of dissolution

and precipitation reactions. 4.4 nanometers is within our integrated ^{12}C measurement of 3.3-9.1 nanometers of ^{12}C-calcite added in SIMS experiments at $\Omega = 1.3$. The model thus confirms our SIMS measurements are accurately measuring the amount of precipitation in the solid, and gives us confidence in our measurement of the ^{12}C enrichment in our undersaturated experiments.

Dissolution-Precipitation Box Model and Data Fitting

Box Model

We developed a box model of dissolution and precipitation at the mineral surface to model our raw data of ^{13}C versus time. A schematic of this model is shown in Figure S4. The model has three main reservoirs: The bulk solution, a boundary layer, and a reactive calcite layer. Carbon from the bulk solution diffuses into and out of the boundary layer. Dissolution and precipitation reactions occur between the boundary layer and the reactive calcite layer. Because so little calcite is dissolved in our experiments, we keep the total surface area reacting with seawater fixed over time. We model this reactive calcite layer as a fixed volume "reaction front" that is constantly in contact with seawater, calculated as the fixed total surface area multiplied by a reactive layer thickness. In order to keep this volume fixed through time in the model, material removed by dissolution must be replaced by an equal flux of material from the calcite interior into the reaction front:

$$\frac{d[^{13}\mathrm{C}]_{bulk}}{dt} = D\frac{SA}{l}\left([^{13}\mathrm{C}]_{bl} - [^{13}\mathrm{C}]_{bulk}\right)\frac{1}{V_{bulk}}; \tag{4a}$$

$$\frac{d[^{12}\mathrm{C}]_{bulk}}{dt} = D\frac{SA}{l}\left([^{12}\mathrm{C}]_{bl} - [^{12}\mathrm{C}]_{bulk}\right)\frac{1}{V_{bulk}}; \tag{4b}$$

$$\frac{d[^{13}\mathrm{C}]_{bl}}{dt} = \left(D\frac{SA}{l}\left([^{13}\mathrm{C}]_{bulk} - [^{13}\mathrm{C}]_{bl}\right) + R_{diss}\cdot f^{13}_{solid} - R_{precip}\cdot f^{13}_{bl}\right)\frac{1}{V_{bl}}; \tag{4c}$$

$$\frac{d[^{12}\mathrm{C}]_{bl}}{dt} = \left(D\frac{SA}{l}\left([^{12}\mathrm{C}]_{bulk} - [^{12}\mathrm{C}]_{bl}\right) + R_{diss}\cdot f^{12}_{solid} - R_{precip}\cdot f^{12}_{bl}\right)\frac{1}{V_{bl}}; \tag{4d}$$

$$\frac{d[^{13}\mathrm{C}]_{solid}}{dt} = R_{precip}\cdot f^{13}_{bl} - R_{diss}\cdot f^{13}_{solid} + (R_{diss} - R_{precip})\cdot f^{13}_{interior}; \tag{4e}$$

$$\frac{d[^{12}\mathrm{C}]_{solid}}{dt} = R_{precip}\cdot f^{12}_{bl} - R_{diss}\cdot f^{12}_{solid} + (R_{diss} - R_{precip})\cdot f^{12}_{interior}. \tag{4f}$$

Fluxes in solution (Eqs. 4a-4d) were calculated in units of concentration per time (moles m^{-3} sec^{-1}). The subscripts *bulk* and *bl* correspond to the bulk solution and diffusive boundary layer reservoirs, respectively. Fluxes into and out of the solid (Eqs. 4e-4f) were calculated in units of moles per time. f^i represent the isotopic mole fractions of stable carbon isotope i. Rates of precipitation (R_{precip}) and dissolution (R_{diss}) are in units of moles per time, and represent the total amount of precipitation or dissolution. The third terms in Eqs. 4e and 4f model the supply of new calcite from the interior, at a rate equal to the net dissolution rate ($R_{diss} - R_{precip}$). This material carries an isotopic composition of the calcite interior. In this case our calcite is pure ^{13}C, so $f^{13}_{interior} = 1$ and $f^{12}_{interior} = 0$.

The following mass balance constraints were applied to the above differential equations:

$$N_{solid,total} = \frac{m_{calcite} \cdot SA_{calcite} \cdot z_{mono} \cdot n_{mono} \cdot \rho_{calcite}}{mm_{calcite}}; \tag{5a}$$

$$f^{13}_{solid} = \frac{N^{13}_{solid}}{N_{solid,total}}; \tag{5b}$$

$$f^{12}_{solid} = 1 - f^{13}_{solid}; \tag{5c}$$

$$V_{bl} = SA_{calcite} \cdot z_{bl}; \tag{5d}$$

$$f^{13}_{bl} = \frac{[^{13}\mathrm{C}]_{bl}}{[^{13}\mathrm{C}]_{bl} + [^{12}\mathrm{C}]_{bl}}; \tag{5e}$$

$$f^{12}_{bl} = 1 - f^{13}_{bl}, \tag{5f}$$

where $N_{solid,total}$ is the total number of moles in the reactive calcite layer; V_{bl} is the volume in cubic meters of the boundary layer and is equal to the calcite surface area $SA_{calcite}$ multiplied by the boundary layer thickness l, assumed to be 10μm. $SA_{calcite} = 0.09$ m^{2}g^{-1} was measured using Kr-BET (Subhas et al., 2015). The thickness of a monolayer of calcite was assumed to be z_{mono}=0.5 nm, and the number of monolayers n_{mono} was varied as discussed below to change the overall volume of calcite reacting with solution. $mm_{calcite} = 100$ g mol^{-1} is the molar mass of calcite and $\rho_{calcite} = 2.63$ g cm^{-3} is its density.

The bulk volume used is identical to our experimental conditions (300 grams of seawater at density 1025 kg m^{-3}).R$_{precip} = R_{diss}/r_{fb}$, the ratio of dissolution to precipitation, which varied between 1.001 to 10 or more (see below for model-data fitting). The model was developed and run in MATLAB r2015a. If the boundary layer l is very thick, diffusion out of the boundary layer restricts the expression of the curvature in the bulk data (not shown), because the initial burst of ^{13}C-labeled DIC is slowly released and mixed out of the boundary layer, rather than being delivered to the bulk solution immediately. However, we expect our boundary layer to be relatively thin and do not expect diffusion to be a major component of our observed rates. This is because mixing rate does not affect our measured dissolution rates between 60-90 rpm. A 10μm boundary layer and the carbonate ion diffusion coefficient in seawater ($9.55{\cdot}10^{-10}$ m^{2}s^{-1}, Li and Gregory (1974)) expresses the curvature in δ^{13}C versus time in both the boundary layer and the bulk solution. Example model output data, taken from the same model run as Figure 2a in the main text, is shown in Figure S5 for the bulk solution, boundary layer, and solid reactive calcite reservoirs. The curvature in all three plots corresponds to the solid calcite layer coming into steady state with respect to the dissolution and precipitation fluxes.

A mass balance can also be constructed for the Mg/Ca of calcite in solution using similar

equations to Eq.(4):

$$\frac{d[\mathrm{Mg^{2+}}]_{bulk}}{dt} = D\frac{SA}{l}\left([\mathrm{Mg^{2+}}]_{bl} - [\mathrm{Mg^{2+}}]_{bulk}\right)\frac{1}{V_{bulk}}; \tag{6a}$$

$$\frac{d[\mathrm{Ca^{2+}}]_{bulk}}{dt} = D\frac{SA}{l}\left([\mathrm{Ca^{2+}}]_{bl} - [\mathrm{Ca^{2+}}]_{bulk}\right)\frac{1}{V_{bulk}}; \tag{6b}$$

$$\frac{d[\mathrm{Mg^{2+}}]_{bl}}{dt} = \left(D\frac{SA}{l}\left([\mathrm{Mg^{2+}}]_{bulk} - [\mathrm{Mg^{2+}}]_{bl}\right) + R_{diss}\cdot f_{solid}^{\mathrm{Mg^{2+}}} - R_{precip}\cdot f_{bl}^{\mathrm{Mg^{2+}}}\right)\frac{1}{V_{bl}}; \tag{6c}$$

$$\frac{d[\mathrm{Ca^{2+}}]_{bl}}{dt} = \left(D\frac{SA}{l}\left([\mathrm{Ca^{2+}}]_{bulk} - [\mathrm{Ca^{2+}}]_{bl}\right) + R_{diss}\cdot f_{solid}^{\mathrm{Ca^{2+}}} - R_{precip}\cdot f_{bl}^{\mathrm{Ca^{2+}}}\right)\frac{1}{V_{bl}}; \tag{6d}$$

$$\frac{d[\mathrm{Mg^{2+}}]_{solid}}{dt} = R_{precip}\cdot f_{bl}^{\mathrm{Mg^{2+}}} - R_{diss}\cdot f_{solid}^{\mathrm{Mg^{2+}}} + (R_{diss} - R_{precip})\cdot f_{interior}^{\mathrm{Mg^{2+}}}, \tag{6e}$$

$$\frac{d[\mathrm{Ca^{2+}}]_{solid}}{dt} = R_{precip}\cdot f_{bl}^{\mathrm{Ca^{2+}}} - R_{diss}\cdot f_{solid}^{\mathrm{Ca^{2+}}} + (R_{diss} - R_{precip})\cdot f_{interior}^{\mathrm{Ca^{2+}}}, \tag{6f}$$

Where $f_i^{\mathrm{Me^{2+}}}$ is the mole fraction of either $\mathrm{Mg^{2+}}$ or $\mathrm{Ca^{2+}}$ in the reservoir i. As in Eq.(4), solution fluxes are in terms of concentration (moles per volume), and solid fluxes are in terms of total moles. R_{diss} and R_{precip} are the total rates of dissolution and precipitation, respectively, in units of moles per time. Incorporation of $\mathrm{Mg^{2+}}$ into the solid is sensitive to the ratio of magnesium to calcium in solution, and the distribution coefficient of magnesium into calcite. We modified $f_{bl}^{\mathrm{Mg^{2+}}}$ such that it represents the mole fraction of magnesium precipitated from the solution:

$$f_{bl}^{\mathrm{Mg^{2+}}} = \frac{D_{Mg}\cdot(\mathrm{Mg/Ca})_{bl}}{1 + D_{Mg}\cdot(\mathrm{Mg/Ca})_{bl}}. \tag{7}$$

Here, $\mathrm{D}_{Mg} = (\mathrm{Mg/Ca})_{solid}/(\mathrm{Mg/Ca})_{bulksolution} = 0.019$ (Oomori et al., 1987) is the distribution coefficient of $\mathrm{Mg^{2+}}$ into calcite at room temperature, and $(\mathrm{Mg/Ca})_{bl}$ is the Mg/Ca ratio in the model boundary layer. The quantity $D_{Mg}\cdot(\mathrm{Mg/Ca})_{bl}$ is thus the Mg/Ca ratio of the precipitated solid in equilibrium with calcite. The right hand side of this equation converts mole ratio to mole fraction, analogous to converting carbon isotope ratios into carbon isotope mole fractions. Implicit in this equation is the assumption that at every model time step, calcite is precipitating in equilibrium with the solution. Implementation of cation mass balance in the model is also shown in Figure S5. As expected, the Mg/Ca ratio of the solid decreases as dissolution overtakes precipitation. At equilibrium, the solid $\mathrm{Mg/Ca} = D_{Mg}\cdot(\mathrm{Mg/Ca})_{bulk} \sim 0.09$.

Data Fitting Using the Box Model Output

Data fitting was performed using the grid search method. A large model parameter space was generated, and data were compared to all model runs over the entire parameter range. The model was initialized and run for 400 values of R_{diss} and 400 values of r_{fb}, spanning multiple orders of magnitude of dissolution rate (10^{-13} to 10^{-8} moles/s), and varying r_{fb} from 1.001-10 (in the framework above, 1-Ω from $\sim$0.009 to 0.9). The time-evolution of each of these model runs (i.e. moles dissolved versus time) was then stored. Experimental data were screened to make sure that there was sufficient data density to provide good constraints on dataset curvature. For

each experiment, the initial data point was set to zero moles dissolved, to eliminate excess δ^{13}C increase that may have occured due to fine particle dissolution. Model data were interpolated to the time values of the experimental data points, and the normalized fitting parameter F was calculated as:

$$nF = \frac{m_{net} - m_{m,net}}{m_{net}} + \frac{1}{i}\sum_{t=0}^{i}\frac{|n_t - n_{m,t}|}{n_t}; \tag{8}$$

where in the first term, m_{net} is the experimentally determined net rate, and $m_{m,net}$ is the modeled net rate, calculated as:

$$m_{m,net} = R_{diss} - R_{precip} = R_{diss} - \frac{R_{diss}}{r_{fb}} = R_{diss}(1 - \frac{1}{r_{fb}}), \tag{9}$$

where R_{diss} and r_{fb} are defined as above. In the second term, n_t are the measured number of moles dissolved at time points 0 to i, and $n_{m,t}$ are the model-calculated moles dissolved at the interpolated time points 0 to i. A normalized fitting parameter was used to avoid bias in the fitting routine arising from differences in the absolute magnitude of dissolution. The implicit assumption of these two terms is that they are both weighted equally in calculating the fitting parameter nF. The fitting parameter was calculated for each dataset at all 400x400 values of R_{diss} and r_{fb}. The best-fitting values of R_{diss} and r_{fb} to each experiment dataset were then found by identifying the R_{diss} and r_{fb} values which gave the lowest fitting parameter nF. Values were chosen as acceptable fits if they fell within 0.3 log units of the global log10(nF) minimum.

Two examples of data-model fits – one closer to equilibrium, and one farther from equilibrium – are shown in Figure S6. A contour plot of log nF versus F_{diss} and r_{fb} is shown in Figure S6b. Panel **a** shows a profile of lognF as a function of r_{fb} at the best-fit value of logR_{diss} (red line), and a profile of lognF as a function of r_{fb} along the covarying path of the local minimum through model space (black line). Panel **d** shows nF across the entire model space. Panel **e** shows a profile of lognF as a function of R_{diss} at the best-fit value of r_{fb} (red line), and a profile of lognF as a function of R_{diss} along the covarying path of the local minimum through model space (black line). The best model fits typically had errors on the order of 10% or less, which are comparable to the $\sim$ 5% errors in experimental dissolution rate determinations (Subhas et al. (2015)). R_{diss} and r_{fb} values were then binned based on the goodness of fit, and statistics were collected on all R_{diss} and r_fb pairs that were within 0.3 log units of the global nF minimum. These best fits are found along the black-dashed line in Figure S6b. The distributions of F_{diss} and r_{fb} look very different for the two experiments in Figure S6. The high dissolution rate experiment has a much longer tail in both F_{diss} and in r_{fb}, which indicates a large range in both of these parameters that can adequately fit the data. Comparatively, the low undersaturation experiment demonstrates a tighter distribution of F_{diss} and r_{fb} values, although there are a few fliers at high dissolution rate that are paired with very low r(fb) values. We acknowledge that the fit to the lower undersaturation experiment is systematically off, and there is still curvature in this dataset that is not explained by the model. The suggestion of an underconstrained saturation state is reasonable, but our experiments are designed to minimize changes in Ω during a dissolution experiment. Both δ^{13}C and alkalinity provide measured constraints on the magnitude of Ω before, during, and after a dissolution experiments. For high undersaturation

experiments where dissolution rate is fast, we run our experiment for less time, and monitor *in situ* alkalinity changes due to dissolution. These changes result in at most a 0.03 change in Ω over the course of a dissolution experiment. Thus we discount large changes in Ω affecting our data from the perspective of our experimental design and our measurements of dissolution rate and saturation state. Furthermore, the a change in Ω would affect the high dissolution rate data more than the low dissolution rate data, and thus cannot be the source of all curvature in our data sets, as near-equilibrium data sets are more curved than far from equilibrium data sets.

There is one other explanation for small curvature farther from equilibrium. The amount of curvature expressed in the model is a function of the size of the fluxes relative to the size of the reactive layer. At higher dissolution rate, the fluxes quickly reset the reactive layer and thus very little curvature is expressed. Therefore, for this high net rate, there is very little curvature in the model values that can fit this data set. One explanation for for the change in curvature near $\Omega = 0.7$ is that when the mechanism switches, the reactive layer deepens. Onset of 2D nucleation across the entire mineral surface could indeed lead to a deepening of the reaction front into the calcite lattice, as now the entire calcite surface is activated for dissolution. However, as discussed in the main text, activation of the entire surface for dissolution also means that precipitation reactions will have less of an influence on the isotopic composition of the solid, as any precipitation should be immediately removed through re-dissolution. Given these caveats, we conclude that the data fits using our model are valid, and continue with the interpretation of our net rate data presented in the main text. All model files are available upon request to the corresponding author.

Sensitivity to Various Model Parameters

Apart from R_{diss} and r_{fb}, the main model sensitivity is in the number of monolayers of calcite (0.5 nm thick) that are allowed to react with solution. This parameter determines the shape and strength of the curvature, and also affects the ability of the model to fit the dissolution rate data. Figure S7 shows the goodness of fit for several different reactive layer thicknesses (1, 3, 5, and 7 monolayers) as quartile box plots. The red line is the median of the misfit. Edges of the boxes are the 25th and 75th percentiles. The whiskers include the data extremes and outliers are plotted as red crosses. 5 monolayers provides the best overall misfit to the dataset. The box model fits are slightly skewed: they are not evenly distributed around the mean misfit value. This is partially because there is a floor at 0% misfit. But also, this skewness suggests that there are high-misfit outliers. These higher misfits are due to δ^{13}C curvature that cannot be explained using our fixed saturation-state box model and thus lead to a larger misfit in the δ^{13}C versus time data. In Subhas et al. (2015), we calculated mean Ω values and rates for these experiments; here, our model does not adjust its dissolution rate as a function of saturation state. We thus attribute these highest misfits as a consequence of small changes in Ω, through either DIC loss or alkalinity generation at high rates of dissolution, leading to a changing dissolution rate over the course of the experiment. The misfit percentage does not scale with Ω, suggesting that our data is not biased by an inability to sufficiently fit data as a function of saturation state. Based on the overall ability of the model to fit all of our dissolution data, we chose a reactive layer thickness of 5 monolayers in our model, which was further justified through the SIMS experiments described and discussed above and in the main text. More than 7 monolayers starts to become inconsistent

with the tracer incorporation measured via SIMS, as discussed above.

Expressions for the Dissolution Rate of Calcite

The canonical derivation of a linear dissolution rate law for calcium carbonate

Eq. 1 in the main text is a canonical representation of dissolution kinetics, and is the basis for framing dissolution in terms of undersaturation, or 1-Ω:

$$R_{net} = R_f - R_b = k_f\{\mathrm{CaCO_3}\} - k_b[\mathrm{Ca^{2+}}][\mathrm{CO_3^{2-}}] = k_f - k_b[\mathrm{Ca^{2+}}][\mathrm{CO_3^{2-}}], \tag{10}$$

where R_{net} is in units of moles per time, k_f is in units of moles per time, and k_b is in units of length[6] mole^{-1} time^{-1}. Assuming that the activity of the carbonate solid is 1, $R_f = k_f$ and $R_b = k_b[\mathrm{Ca^{2+}}][\mathrm{CO_3^{2-}}]$. Substitution of $K'_{sp} = \frac{[\mathrm{Ca^{2+}}][\mathrm{CO_3^{2-}}]_{sat}}{\{\mathrm{CaCO_3}\}} = \frac{k_f}{k_b}$ into Eq.(10), and the definition of $\Omega = \frac{[\mathrm{Ca^{2+}}][\mathrm{CO_3^{2-}}]}{K'_{sp}}$, gives:

$$R_{diss} = k_r \cdot K'_{sp} - k_r[\mathrm{Ca^{2+}}][\mathrm{CO_3^{2-}}] = k_r \cdot K'_{sp}(1-\Omega) = k_{diss}(1-\Omega). \tag{11}$$

Here, k_{diss} is in units of moles per time. Dividing Eq.(11) by surface area gives the specific dissolution rate in units of moles length^{-2} time^{-1}. In addition, this model suggests that the ratio of dissolution and precipitation rates is linearly proportional to Ω:

$$\Omega = \frac{[\mathrm{Ca^{2+}}][\mathrm{CO_3^{2-}}]}{K'_{sp}} = \frac{[\mathrm{Ca^{2+}}][\mathrm{CO_3^{2-}}] \cdot k_r}{k_f} = \frac{R_b}{R_f}. \tag{12}$$

It is important to emphasize that curvature in either the gross rate of dissolution or precipitation – and thus in the net rate of dissolution – as a function of saturation state necessitates nonlinearities in either or both of these terms. For instance, curvature in the gross dissolution rate implies that either the activity of the solid is not unity at all saturation states, or that there are other terms that must be included in the rate law. The inclusion of other terms, for instance carbonic acid as a driver of dissolution, may be the way forward. A fully predictive rate law as a function of chemical specitaion would thus include multiple terms, and would necessitate a speciation model of the calcite surface as a function of dissolved species and the density of calcium and carbonate surface ion sites in seawater.

A derivation of Eq. 3 in the main text

In the last section, we discuss a 2D-nucleation model of calcite dissolution similar to that presented by Dove et al. (2005). This model takes elements of classical growth and nucleation theory and applies them to dissolution. The rate of dissolution initiated by etch pit formation is defined as:

$$R_n = hv^{2/3}J^{1/3}, \tag{13}$$

where the normal dissolution rate R_n is a function of the step height h, the speed of a moving step v, and the steady-state etch pit nucleation rate, J. The nonlinear dependence of R_n

on J is discussed extensively elsewhere (Sangwal, 1987; Malkin et al., 1989). The form of this dependence changes the absolute value of surface energies calculated in Table 1 in the main text; however, it does not impact the trends in surface energy or the location of the rate transition between defect-initiated and homogeneous etch pit nucleation shown in Figure 5 in the main text. The step retreat velocity v depends on solution composition in a formulation similar to Eq.(10) above:

$$v = \omega\beta(C_e - C) = \omega\beta C_e(1 - \Omega); \tag{14}$$

where ω is the molecular volume of calcite, β is the step kinetic coefficient cm/s, and C_e is the equilibrium concentration of the species. In the case of calcite, C_e is equivalent to the K'_{sp} of calcite. J, the frequency of nucleating an etch pit, is related to saturation state $\sigma = \ln\Omega$, as nucleation is activated above some $\Delta G_{critical}$, defined by the interface free energy barrier to nucleation α:

$$J = |\sigma|^{1/2} n_s a h C_e \beta \exp\left[\frac{\pi\alpha^2\omega h}{(k_B T)^2}\left|\frac{1}{\sigma}\right|\right]. \tag{15}$$

New terms here are the lattice spacing a and the density of nucleation sites n_s. Substituting Equations 15 and 14 into Eq.(13) and rearranging for $1/\sigma$, we recover Equation 3 in the main text.

Carbonic Anhydrase and its Effect on Dissolution Kinetics

The dissolution rate method from Subhas et al. (2015) allows for sensitive rate determinations in the absence of significant changes of solution chemistry or mineral surface area. For instance, using a 100% labeled $CaCO_3$ solid, we achieve a $\delta^{13}C$ sensitivity of about 20‰ per 1 μeq/kg alkalinity change. Saturation state was determined using DIC-Alk pairs measured on a Picarro CRDS and a home-built titration system. Final errors on Ω, calculated using Alkalinity-DIC pairs, range from $\leq$0.01 to $\sim$0.03 units. The K'_{sp} for calcite was adjusted so that the most saturated dissolution experiments are undersaturated, requiring a correction factor of about 1.03 to the value found in Morse et al. (1980). The alkalinity contribution of carbonic anhydrase ($\sim$30 equivalents/mol) to solutions was determined by a standard additions alkalinity experiment in natural seawater. At the same saturation state (Ω=0.83), curves of $\delta^{13}C$ increase significantly in slope as CA increases (Figure S8).

To test the effect of other proteinaceous material on the rate of calcite dissolution, experiments were conducted in the presence of Bovine Serum Albumin (BSA) at concentrations of 0.002 (not shown) and 0.01 mg/mL (shown in Figure S9 versus uncatalyzed and catalyzed dissolution rates at [CA] = 0.01 mg/mL). These experiments show no significant change in the BSA rate versus the uncatalyzed rate while dissolution experiments in the presence of CA are always faster than those without CA. If anything, rates in the presence of BSA are slightly slower. The behavior of dissolution rate versus ΔG is very similar to that described by Arvidson and Lüttge (2010). In their experiments, surfaces with different amounts of etching were exposed to solutions of similar undersaturation. These surfaces dissolved at significantly different rates,

suggesting that the surface itself exerts significant influence on the relationship between dissolution rate and saturation state. Here, in contrast, it is the presence of CA, instead of a surface feature hysteresis, driving a different functional dependence between ΔG and dissolution rate.

Figures and Tables

Profile Type	$^{12}C/^{13}C$	Mg/Ca
Beam type	Cesium	Oxygen
Sample HV	-5 kV	-8.5 kV
Aperture	300 μm	300 μm
Raster size	50x50 μm	50x50 μm
Beam current	0.5 nA	3 nA
Incidence Angle	24.5°	22.5°
Mass Resolution Δm/m	3,000	2,000

Table S1: Pertinent information for SIMS profile analysis on the CAMECA 7f instrument.

	$\Omega = 0.95$	$\Omega = 1.3$
$^{12}C_{tot}$	0.7-2.2·10^{-13}	2.1-6.3·10^{-13}
$Mg^{2+}{}_{tot}$	1.5-7.8·10^{-15}	1.3-8.8·10^{-15}
$z_{eff,^{12}C}$ (nm)	1.0-3.3	3.1-9.3
$z_{eff,Mg}$ (nm)	0.3-1.5	0.2-1.7

Table S2: Estimates of new tracer incorporation based on integration of $^{12}C/^{13}C$ and Mg/Ca SIMS profiles. The number of moles added were determined using Eq.(1) of SIMS profile data. This was then converted to a thickness of calcite as described in the text.

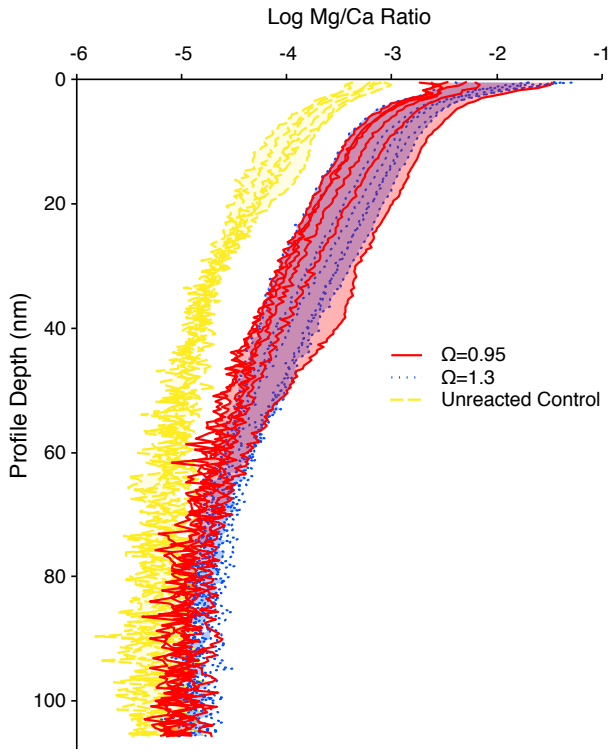

Figure S1: SIMS Mg/Ca profiles for the same experimental conditions as the main text. Ratios were collected as $^{40}Mg^{2+}/^{24}Ca^{2+}$, and demonstrate a measurable incorporation of Mg into calcite in both undersaturated and supersaturated conditions.

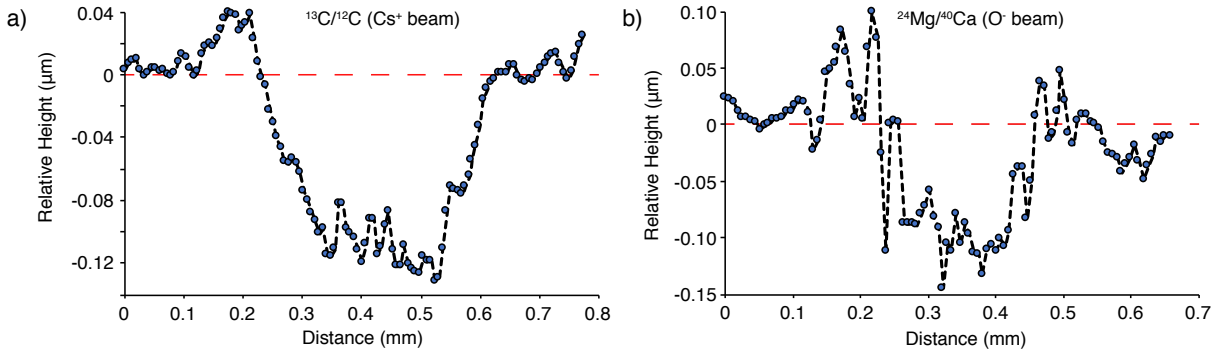

Figure S2: Example of SIMS analysis pits measured on a profilometer for the **a)** cesium beam and **b)** oxygen beam. Pits are different profiles measured on the same calcite grain. Profiles have been smoothed using a 3-point moving average for clarity, are are plotted relative to an arbitrarily designed zero height. Note the increased roughness in the oxygen profile relative to cesium.

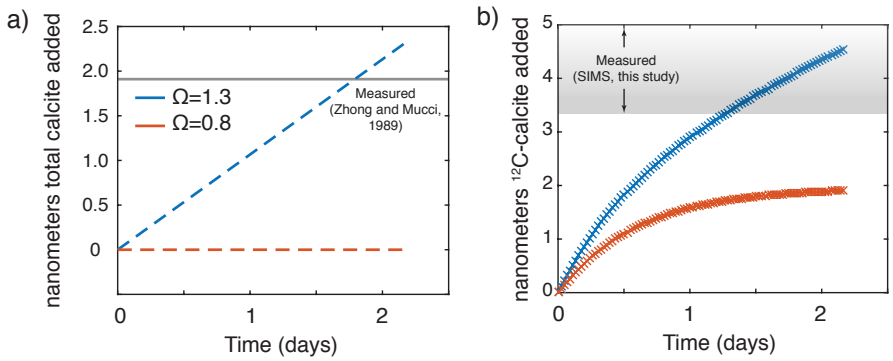

Figure S3: Plots of the dissolution-precipitation box model run in "precipitation mode" ($R_{precip}/R_{diss} = 1.3$, blue lines) over 2 days, such that calcite of seawater δ^{13}C composition was added to the surface. For comparison, a dissolution model run is also shown ($R_{precip}/R_{diss} = 0.8$, red lines). **a)**; The total thickness of calcite added to the reactive surface. Net precipitation adds calcite to the reactive surface; net dissolution does not. The amount of net precipitation in 48 hours as measured by Zhong and Mucci (1989) is shown as a grey line for reference. **b)**; the effective thickness (z_{eff}) of pure ^{12}C calcite added to the reactive surface. Both curves add ^{12}C to the solid, due to active gross precipitation under both saturation states. Much more ^{12}C is added during net precipitation. Using a ratio of precipitation to dissolution of 1.3 and a net precipitation rate of 1 μmol m^{-2} hr^{-1} gives a correct total thickness of calcite added, and furthermore shows that there is more addition of $^{12}\text{C} - \text{CaCO}_3$ than total CaCO_3, due to dissolution-reprecipitation reactions. The range of $^{12}\text{C} - \text{CaCO}_3$ measured in SIMS experiments described above is shown in the shaded box for reference.

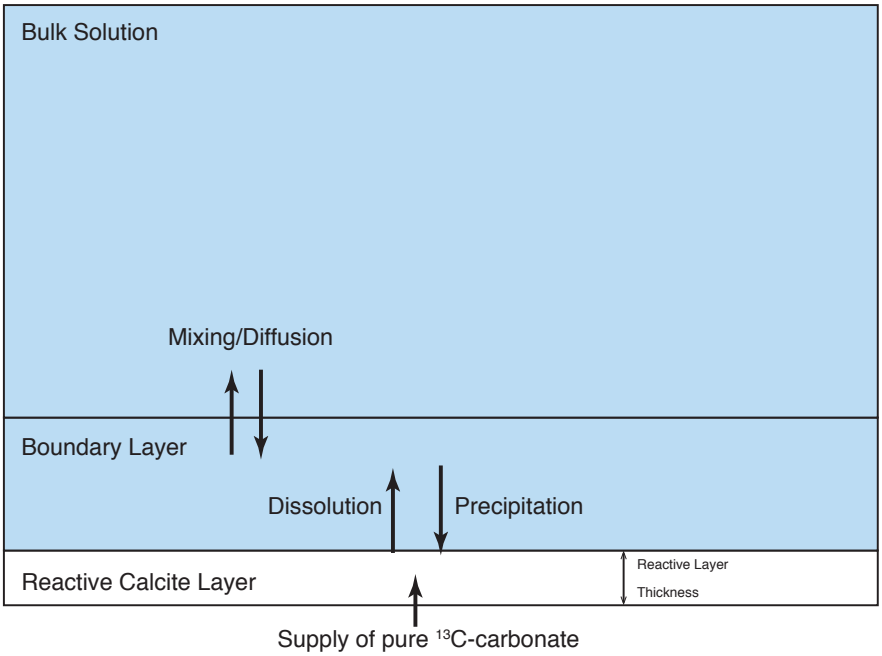

Figure S4: A schematic of our dissolution-precipitation box model. The number of monolayers changes the size of the "reactive calcite layer" reservoir. This fixed-volume reservoir is supplied with pure ^{13}C carbon at a rate equal to the amount eroded due to net dissolution, as described in Eq.(4).

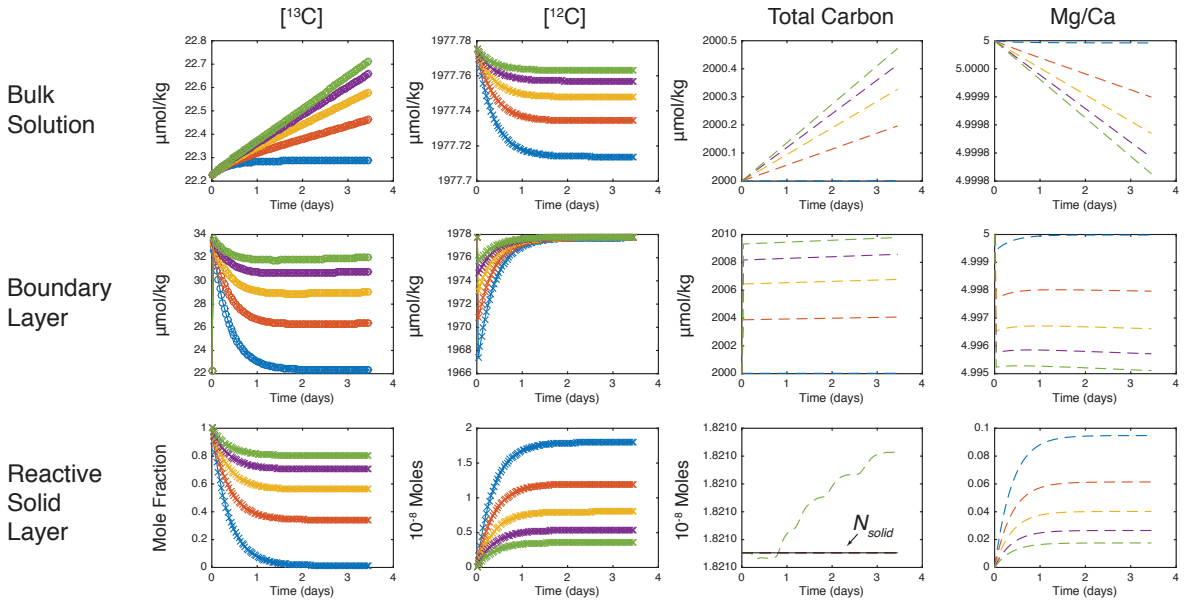

Figure S5: Example box model output showing the isotopic evolution and mass balance of the bulk solution (top row), boundary layer (middle row), and reactive calcite layer (bottom row) reservoirs. Different curves were generated by fixing k_{diss} and varying r_{fb} from 1 to 5. This data was taken from the same model run as the data in Figure 2a in the main text. Color key is the same as the main text figure; i.e. r_{fb} for blue = 1.0; red = 1.5; yellow = 2.2; purple = 3.4; and green = 5.0. For total carbon in the reactive calcite layer, the initial number of moles in the model (N_{solid}) is indicated as a solid black line. With complete mass balance, all model runs should not deviate from this initial value. The green experiment showed some numerical drift; however, this drift is small (less than 0.001 nanomoles). All other experiments showed no deviation from the initial value of N_{solid}.

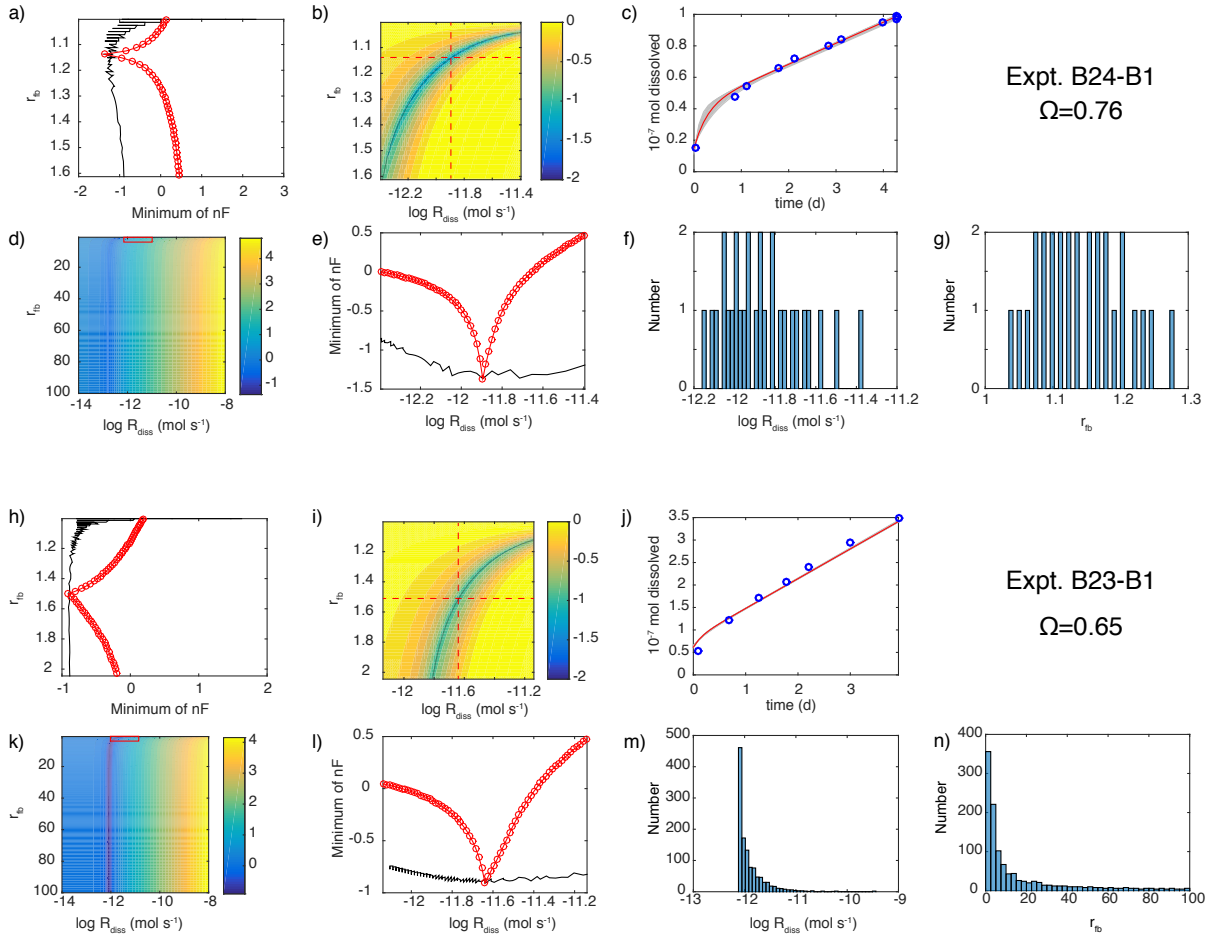

Figure S6: An example of the model-data fitting routine output for two dissolution experiments. **a-g**); data-model fits for an experiment conducted at $1-\Omega = 0.24$. **b)**; The surface of model-data misfit plotted as $\log nF$, zoomed in on the values of r_{fb} (ratio of gross dissolution to precipitation) and F_{diss} (gross dissolution rate constant) that minimize $\log nF$. Low values indicate a better overall misfit: -1 corresponds to a 10^{-1} or 10% error in the fit. Red dashed lines intersect at the global minimum pair of F_{diss} and r_{fb}. The black dashed line follows the covarying path of the local minimum in the cost function. Values of F_{diss} and r_{fb} along the black traces allow for the calculation of statistics on the fit. Panel **a)** shows a profile of $\log nF$ for r_{fb} values at a fixed value of F_{diss} (red line with points, i.e. following the dashed vertical line in panel **b**), and along the local minimum trace of nF (black line, i.e. following the curved black line in panel **b**). **d)** shows the entire parameter space, with a small rectangle indicating the zoomed region in panel **b**. Note the change in color scale for values of $\log nF$. Panel **e)** shows a profile of $\log nF$ for the entire range of F_{diss} values at a fixed value of r_{fb} (red line with points) and along the local minimum trace (black line). Panel **c** shows the data-model misfit for the top model parameters F_{diss} and r_{fb}. Panels **f** and **g** show histograms of the best-fit values for F_{diss} and r_{fb}, respectively. **h-n**); The same panels as above for an experiment run at $1-\Omega = 0.35$. Note that the number of acceptable fits in panels **m** and **n** is much larger, as are the ranges in both F_{diss} and r_{fb}. Also note that the large peak in R_{diss} must correspond to the long tail of large r_{fb} values, in order to satisfy the constraint on the net rate. This range is also evident in the relatively flat black curves in panels **h** and **l**. These distributions are the basis for the range limits in Figure 3 in the main text.

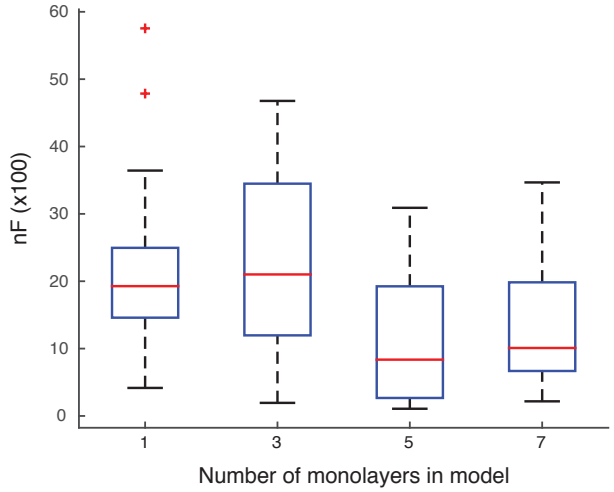

Figure S7: Sensitivity test of mean model goodness of fit (in %) for all experiments as a function of the number of monolayers in the reactive calcite reservoir, plotted as box plot quartiles. The y-axis is the misfit parameter nF multiplied by 100. The red line is the median of the misfit. Edges of the boxes are the 25th and 75th percentiles. The whiskers include the data extremes and outliers are plotted as red crosses. There is a minimum in the misfit error if 5 monolayers of calcite are used.

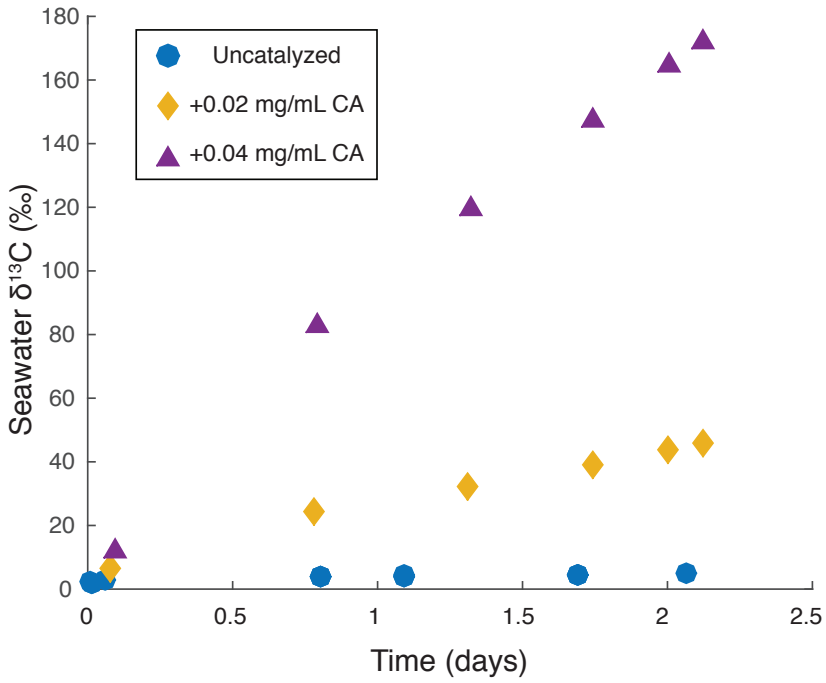

Figure S8: Plots of δ^{13}C verus time for several dissoltion experiments at the same saturation state and different [CA].

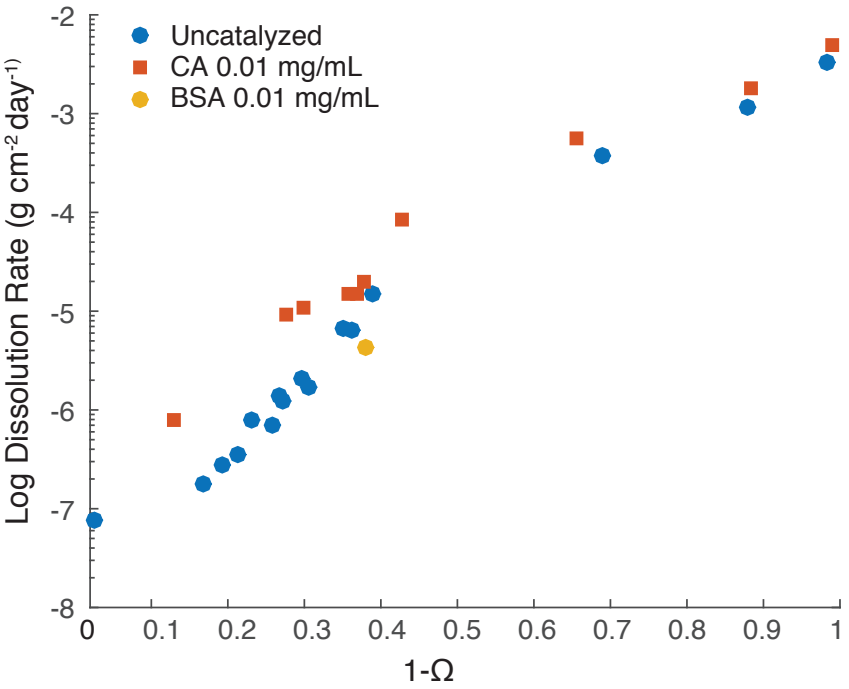

Figure S9: Dissolution rates in the presence of BSA compared to uncatalyzed dissolution rates at the same undersaturation. The similarity in rate indicates that unreactive dissolved organic matter has no influence on dissolution rate.

References

Arvidson, R. S. and A. Lüttge, 2010: Mineral dissolution kinetics as a function of distance from equilibrium – New experimental results. *Chemical Geology*, **269(1-2)**, 79–88.

Dove, P. M., N. Z. Han, and J. J. De Yoreo, 2005: Mechanisms of classical crystal growth theory explain quartz and silicate dissolution behavior. *Proceedings of the National Academy of Sciences*, **102(43)**, 15357–15362.

Li, Y. H. and S. Gregory, 1974: Diffusion of Ions in Sea-Water and in Deep-Sea Sediments. *Geochimica et Cosmochimica Acta*, **38(5)**, 703–714.

Malkin, A. I., A. A. Chernov, and I. V. Alexeev, 1989: Growth of Dipyramidal Face of Dislocation-Free Adp Crystals - Free-Energy of Steps. *Journal of Crystal Growth*, **97(3-4)**, 765–769.

Morse, J. W., A. Mucci, and F. J. Millero, 1980: The solubility of calcite and aragonite in seawater of 35%. salinity at 25 C and atmospheric pressure. *Geochimica et Cosmochimica Acta*, **44**, 85–94.

Morse, J. W., Q. Wang, and M. Y. Tsio, 1997: Influences of temperature and Mg:Ca ratio on $CaCO_3$ precipitates from seawater. *Geology*, **25(1)**, 85–87.

Mucci, A. and J. W. Morse, 1984: The solubility of calcite in seawater solutions of various magnesium concentration, It= 0.697 m at 25 C and one atmosphere total pressure. *Geochimica et Cosmochimica Acta*, **48**, 815–822.

Oomori, T., H. Kaneshima, Y. Maezato, and Y. Kitano, 1987: Distribution Coefficient of Mg^{2+} Ions Between Calcite and Solution at 10-50 Degrees C. *Marine Chemistry*, **20(4)**, 327–336.

Sangwal, K., 1987: *Etching of Crystals: Theory, Experiment, and Application*. North Holland.

Subhas, A. V., N. E. Rollins, W. M. Berelson, S. Dong, J. Erez, and J. F. Adkins, 2015: A novel determination of calcite dissolution kinetics in seawater. *Geochimica et Cosmochimica Acta*, **170(C)**, 51–68.

Sun, W., S. Jayaraman, W. Chen, K. A. Persson, and G. Ceder, 2015: Nucleation of metastable aragonite $CaCO_3$ in seawater. *Proceedings of the National Academy of Sciences*, **112(11)**, 3199–3204.

Zhong, S. and A. Mucci, 1989: Calcite and aragonite precipitation from seawater solutions of various salinities: Precipitation rates and overgrowth compositions. *Chemical Geology*, **78(3-4)**, 283–299.